Microwave Engineering
Ulm University

universität
ulm

Probabilistic SAR Processing for High-Resolution Mapping using Millimeter-Wave Radar Sensors

Timo Grebner, Alexander Grathwohl, Pirmin Schoeder, Vinzenz Janoudi, Christian Waldschmidt

© 2023 IEEE. Personal use of this material is permitted. Permission from IEEE must be obtained for all other uses, in any current or future media, including reprinting/republishing this material for advertising or promotional purposes, creating new collective works, for resale or redistribution to servers or lists, or reuse of any copyrighted component of this work in other works.
DOI: 10.1109/TAES.2023.3289784

Probabilistic SAR Processing for High-Resolution Mapping using Millimeter-Wave Radar Sensors

Timo Grebner, Graduate Student Member, IEEE
Institute of Microwave Engineering, Ulm University

Alexander Grathwohl, Graduate Student Member, IEEE
Institute of Microwave Engineering, Ulm University

Pirmin Schoeder, Graduate Student Member, IEEE
Institute of Microwave Engineering, Ulm University

Vinzenz Janoudi, Graduate Student Member, IEEE
Institute of Microwave Engineering, Ulm University

Christian Waldschmidt, Fellow, IEEE
Institute of Microwave Engineering, Ulm University

***Abstract*— In the field of autonomous driving, highly accurate representations of the environment are essential for trajectory planning as well as for estimating the vehicle's location. Today, this can be achieved with the help of chirp-sequence radar sensors or radar sensor networks. The possibilities for environmental mapping cover simple point clouds, target list based grid maps and raw data based high resolution synthetic aperture radar (SAR) maps. While for target list based grid maps it has already been shown that a probabilistic occupancy grid map has significant advantages over an amplitude-based grid map in terms of robustness and resolution, no probabilistic approaches to SAR processing exist up to now. This paper presents a fundamental approach of processing radar raw data to generate high-resolution SAR images based on probabilities. A probabilistic SAR processing is presented which combines high resolution environmental mapping with amplitude independent target detection. Based on measurements, a qualitative and quantitative comparison between conventional amplitude and phase-based SAR processing, the presented probabilistic SAR processing, and a probabilistic target list-based occupancy grid map is performed. Since the presented algorithm is not limited to the automotive field and chirp-sequence radar sensors, it can be extended to arbitrary SAR applications and radar architectures.**

***Index Terms*— ADAS, chirp-sequence radar sensors, gird-mapping, millimeter wave, occupancy grid-map, probabilistic mapping, radar sensor networks, SAR, synthetic aperture radar**

I. INTRODUCTION

THE increasing progress in the field of autonomous driving demands ever higher requirements on environment recognition and thus on the sensor systems. A variety of sensor systems can be used for this purpose, which differ in their robustness, accuracy and price. While LIDAR systems and cameras offer a high angular resolution [1], they provide poor robustness against weather conditions such as snow, fog and blinding sun [2]. Radar systems, on the other hand, have limited angular resolution due to their reduced aperture size in relation to the wavelength, but are able to detect targets with consistent precision almost regardless of weather conditions, making radar sensors a robust perception system [3], [4]. In recent years, the use of a radar sensor network offers significant advantages in terms of detection capability, and accuracy.

The target information, determined from radar raw data, can be used with the help of different methods for environmental mapping. A fundamental differentiation is being made between point clouds and grid maps [5]. Grid maps offer the advantage of a cell-based representation of the environment, which allows efficient processing in applications based on them.

Grid maps can be generated either based on target lists (T-GM) or on raw data (R-GM) [6]. Target list-based mapping approaches are primarily divided into amplitude grid maps (T-AGM) and probabilistic occupancy grid maps (T-OGM) [7], [8]. In both simulations and measurements, probabilistic occupancy grid maps provided a much more robust representation of the environment with significantly increased resolution. One possibility to represent the environment in a much higher resolution without changing the hardware is a synthetic aperture radar (SAR). Based on the raw data of a mm-wave radar sensor mounted on a moving vehicle, a larger aperture is spanned resulting in increased angular accuracy in comparison to T-GM [6], [9]. Since SAR processing represents the environment in a cell-based manner as well, it is called a raw data-based grid map in the following. In order to combine the raw data of different measurements into a global map of the environment, many SAR approaches exist. The approaches primarily differ in the domain they are processed in.

In general, there is a distinction between processing in the time domain and processing in the frequency domain [10], [11], [12]. However, all of these algorithms ultimately create an amplitude-based representation of the environment (R-AGM). The disadvantage of this approach is the processing which is directly based on the amplitude information and the phase information of the complex measurements. Thus, the dynamic of the resulting map depends significantly on the strongest target and the weakest target. However, the amplitude is not relevant for the environment representation, but only the question whether there is a target at this position or not. Even weakly reflecting obstacles must be mapped regardless of the dynamics of the map. In addition, measurement inaccuracies such as noise or position inaccuracies are not taken into account for conventional SAR processing. These measurement inaccuracies nevertheless have a significant contribution to the measurement results.

The authors are with the Institute of Microwave Engineering, Ulm University, 89081 Ulm, Germany (e-mail: timo.grebner@uni-ulm.de).

0018-9251 © 2020 IEEE

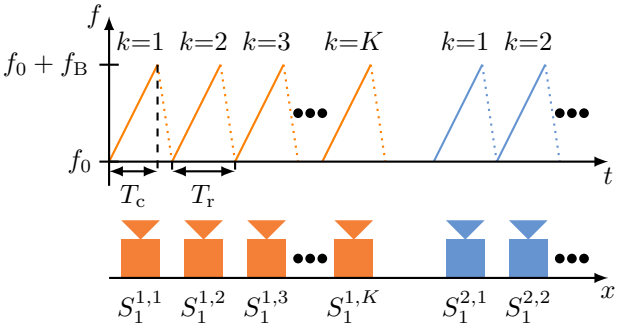

Fig. 1: Top: chirp-sequence modulation scheme for K ramps and two frames (1: orange, 2: blue). Bottom: sensor position for each transmitted ramp spanning a synthetic aperture.

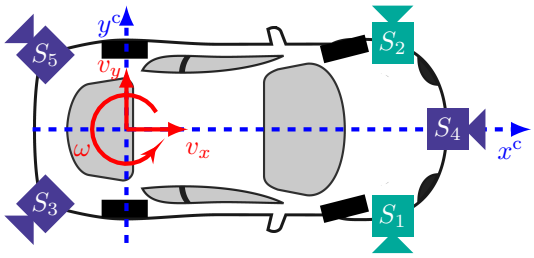

Fig. 2: Exemplary radar network with N=5 radar sensors in violet and turquoise with arbitrary orientations. Vehicle coordinate system [x^c, y^c] in blue, dashed and corresponding velocity components in red, solid lines. Turquoise sensors are used for measurement evaluation.

The presented concept in this work describes a possibility of processing a synthetic aperture with the means of probabilities. In contrast to conventional SAR processing, not only the complex pointers are phase-corrected and added, but probabilistic assumptions are made based on the measurement data and models are created, which subsequently lead to a highly precise image of the environment using probabilistic update rules. The concept presented combines the advantages of raw data based SAR processing, providing high resolution and large integration gain, with the advantages of a probabilistic representation of the environment, its high robustness and its nearly amplitude independent probabilistic representation. Since the final resulting image represents occupancy probabilities for each cell, direct information about free space and obstacles is also provided.

The paper is organized as follows: The sensor setup and the radar architecture are presented in Section II. Subsequently, the signal processing chain for ordinary amplitude-based SAR (A-SAR) and probabilistic SAR (P-SAR) is presented in Section III. The most important equations for conventional SAR processing are derived in Section IV based on the backprojection algorithm. Based on this, in Section V methods for probabilistic SAR processing are inferred, which are evaluated in the Sections VI and VII based on measurements.

II. Concept and System Architecture

The general system architecture comprises distributed incoherently networked MIMO radar sensors. The radar sensors are operated with a chirp-sequence modulation and are only interconnected via a common trigger for rough time synchronization. The radar sensors emit sequences of frequency modulated continuous wave (FMCW) ramps, which have a bandwidth f_B, an up-chirp time T_c, and a ramp repetition time T_r [13], [14]. The radar sensors are frame-based and emit a total of K ramps in each of the W frames. The notations as well as the modulation scheme are illustrated in Fig. 1 for a sensor S_1.

The slope κ of the transmission ramp results from the ratio between the bandwidth f_B and the up-chirp time T_c. The transmission ramp shown in Fig. 1 is described with the following term [15], [16]:

$$s_{\mathrm{Tx}}(t) \propto e^{\mathrm{j}\left(2\pi f_0 t + \pi\kappa t^2 + \phi_0\right)} \tag{1}$$

For reasons of clarity, the amplitude is neglected. This signal is emitted by the transmit antenna of the radar sensor, reflected at a target and then received again with the receive antenna. The propagation time in the channel is described by $\tau = {}^{2r}/_{c_0}$. The distance between the sensor and the target is described by r. The received signal corresponds to the time delayed transmitted signal and is described by

$$s_{\mathrm{Rx}}(t) \propto e^{\mathrm{j}\left(2\pi f_0 (t-\tau) + \pi\kappa (t-\tau)^2 + \phi_0\right)}. \tag{2}$$

The chirp-sequence radar architecture mixes this received signal with the transmitted signal and subsequently low-pass filters it to obtain the IF signal.

$$s_{\mathrm{IF}}(t) \propto e^{\mathrm{j}\left(2\pi f_0 \tau + 2\pi\kappa t\tau - \pi\kappa\tau^2\right)}. \tag{3}$$

For each of the K emitted ramps and W frames, this IF signal is subsequently processed.

Fig. 1 illustrates frame 1 in orange whereas frame 2 in blue. Due to the motion of the vehicle and thus also the motion of the radar sensor, the sensor is located at a different position in the global map $\mathbf{m}$ at each measurement time and spans up a virtual aperture. The measurement time $t^{w,k}$ describes in the following the time at which the k-th ramp of the w-th frame is transmitted. Identically to real antenna apertures, antenna spacings larger $\frac{\lambda}{2}$ lead to increased side lobes even with synthetic apertures [17]. As soon as the synthetic aperture is sampled in equidistant intervals even grating lobes will result. Therefore, ramp repetition time T_r is of great importance for the quality of the resulting SAR image, since it ultimately limits the maximum speed of the vehicle.

The system may include an arbitrary number of radar sensors mounted on a vehicle. Although the sensors are incoherently networked and just synchronized in time, the SAR algorithms can be applied in a cascaded manner to any number of sensors to provide coherent signal addition. A possible sensor configuration is shown in

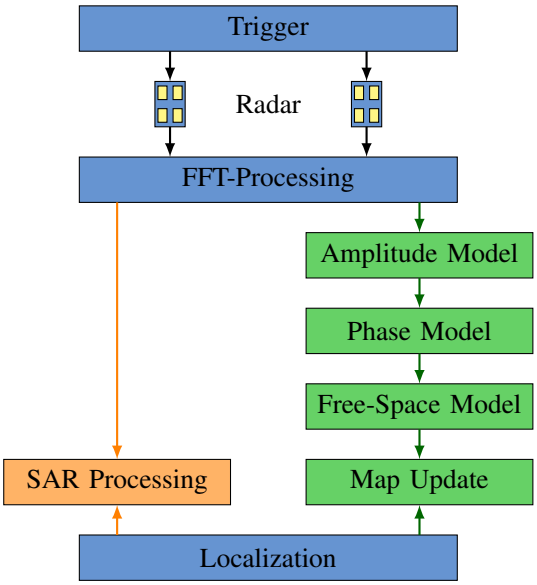

Fig. 3: Signal flow chart for conventional SAR processing (orange) and probabilistic SAR processing (green). Blue boxes indicate general steps used for both applications.

Fig. 2 for $N{=}5$ radar sensors. With side-looking 77 GHz radar sensors, S_1 and S_2, mounted on a vehicle high-resolution environmental mapping is possible [6]. Furthermore, the concept of SAR processing can be applied as well to sensor S_3, S_5, and S_4 and thus to front-looking radar sensors to obtain high-resolution images of the environment in the direction of motion [18].

III. Processing Chain

An overview of the basic signal processing is shown in Fig. 3. The blue blocks indicate general processing steps that are required for both, the conventional amplitude-based SAR and the probabilistic SAR presented in this work. The orange block describes the SAR processing for the amplitude-based SAR. In green, the steps for the probabilistic SAR processing are shown.

In the first step, the raw data samples of the IF signal s_{IF} from N time-synchronized incoherently connected radar sensors are stored. Based on the time samples of each ramp (fast time), the distance information is determined with the help of a range compression and thus a transformation into the frequency domain with a fast Fourier transformation (FFT). This range compression is performed independently for all K ramps of each frame and sensor. Zero-padding is performed in this process for obtaining more accurate amplitude estimates of resolvable signal components. For the sake of clarity, corresponding formulas are derived without zero-padding being applied. Subsequently, the amplitude-based SAR processing is performed in the orange block and the probabilistic SAR processing in the green blocks. The probabilistic SAR is composed of the probabilistic amplitude and phase model as well as the free-space modeling. Based on this modeling, occupancy probabilities can be calculated for each grid cell. These probabilities for each cell of the map are used to update the final map $\mathbf{m}$ with the measured values of the current measurement. This is necessary for the accumulation of different measurements. Ultimately, high-resolution SAR imaging always requires high-precision localization, since at each ramp measurement time the position of each radar sensor must be known to at least $\frac{\lambda}{2}$, which in the automotive sector at frequencies of 77 GHz leads to a required position accuracy of about 1.8 mm [19].

In the following, the general SAR processing is discussed first in order to have a comparison of the signal processing as well as of the results later on. Subsequently, the probabilistic processing steps are discussed. In addition, notations for certain processing steps are introduced, which are also required for probabilistic SAR processing.

IV. Conventional Amplitude SAR Processing

There are many different ways to create SAR images. Mainly, a distinction is made between methods that perform the calculation in the time domain and those that perform the calculation in the frequency domain [10], [11], [12]. However, the basic principle is identical for all these methods. The received and down mixed IF signals are added up according to a matched-filter-based phase correction approach (in the time or frequency domain). For targets, the phases of the signals superimpose constructively in the respective cell, resulting in increased power being received from that cell. For noise, on the other hand, the corrected phases of the signals overlap destructively, so that the cell evaluated represents no or little power and thus is significantly weaker than a real target.

The advantage of time-domain SAR processing is the ability to process the data for arbitrary trajectories without artifacts or linearization. One way to process the data in the time domain for arbitrary trajectories is the backprojection algorithm, which will be used in the following for both conventional amplitude SAR and probabilistic SAR. According to Fig. 3, the SAR processing is based on the samples in the time domain $\mathbf{S}_{\mathrm{IF}}^{w,k}$. For clarity, in the following, measurements are not referenced in relation to the ramps K and frames W but to the measurement time t with $\mathbf{S}_{\mathrm{IF}}^{t}$. These fast time samples are transformed into the frequency domain by means of a 1D FFT

$$\mathbf{A}^t = \mathscr{F}\{\mathbf{S}_{\mathrm{IF}}^t\}, \tag{4}$$

where $\mathbf{A}^t$ describes a vector in the frequency domain, which has the following structure:

$$\mathbf{A}^t = \begin{bmatrix} A_1 & A_2 & \dots & A_{\mathrm{J}} \end{bmatrix}^{\mathrm{T}}. \tag{5}$$

In this case J describes the number of IQ samples of the IF signal of a ramp in the time domain and thus corresponds to the number of frequency points in the frequency domain, if no zero-padding is performed. Each entry of $\mathbf{A}^t$ consists of complex-valued samples for a

certain frequency, which due to the system structure of chirp-sequence radar sensors (3) corresponds to a distance $\mathbf{r}$ and has the following structure:

$$\mathbf{r} = \begin{bmatrix} r_1 & r_2 & \dots & r_\mathrm{J} \end{bmatrix}^\mathrm{T} \tag{6}$$

$$= \begin{bmatrix} 0 & \Delta r & \dots & \Delta r \cdot (J-1) \end{bmatrix}^\mathrm{T}. \tag{7}$$

Δr denotes the range resolution which can be achieved with the radar sensor. Based on this range information $\mathbf{r}$ and the associated complex amplitudes $\mathbf{A}$, SAR processing is performed for the area covered by the matrix $\mathbf{m}$ which describes the environment to be imaged. $\mathbf{m}$ consists of I cells, where m_i represents the i-th cell ($i \leq I$) of $\mathbf{m}$. Each cell m_i is assigned a specific $\mathbf{G}$ by the SAR processing, which represents the integrated received power from that cell. The complex value $\mathbf{G}(m_i)$ of each cell m_i is iteratively calculated using the backprojection algorithm corresponding to [20], [21], [22] with

$$\mathbf{G}\left(m_i|z_{1:\mathrm{t}}, x_{1:\mathrm{t}}\right) = \mathbf{G}\left(m_i|z_{1:\mathrm{t}-1}, x_{1:\mathrm{t}-1}\right) + \mathbf{A}\left(m_i|z_\mathrm{t}, x_\mathrm{t}\right) \cdot \exp\left(\mathrm{j} \cdot \Phi\right). \tag{8}$$

Φ describes the phase correction term to ensure constructive superposition of all complex pointers at the target position and is defined in more detail in (12). During each step, the measurement data of all previous time steps ($1{:}t{-}1$) and the phase corrected measurement data of the current measurement ramp at time t are summed up. Thereby, $\mathbf{x}$ denotes the position and orientation of the vehicle in relation to the global map $\mathbf{m}$, and $\mathbf{z}$ represents the measurement data, which corresponds to the fast time samples. The selection of the correct frequency bin from $\mathbf{A}\left(m_i|z_\mathrm{t}, x_\mathrm{t}\right)$ is performed with

$$\mathbf{A}\left(m_i|z_\mathrm{t}, x_\mathrm{t}\right) = \mathbf{A}^t\left(\mathbf{u}\left(m_i|z_\mathrm{t}, x_\mathrm{t}\right)\right), \tag{9}$$

where $\mathbf{A}^t\left(\mathbf{u}\left(m_i|z_\mathrm{t}, x_\mathrm{t}\right)\right)$ describes the $\mathbf{u}$-th entry of the vector $\mathbf{A}^t$. The assignment $\mathbf{u}$ from a vector to the cell m_i has a similar scheme for all vectors. Therefore, the description is only presented for the vector $\mathbf{A}^t$. The position index $\mathbf{u}$ for the vector $\mathbf{A}^t$ is given by the following ratio rounded to the nearest integer:

$$\mathbf{u}\left(m_i|z_\mathrm{t}, x_\mathrm{t}\right) = \left\lfloor \frac{d_i}{\Delta r} \right\rceil. \tag{10}$$

At this point d_i denotes the distance between the sensor position R_n of the n-th sensor and the cell m_i with

$$d_i = \sqrt{\left(R_{n,x} - m_{i,x}\right)^2 + \left(R_{n,y} - m_{i,y}\right)^2 + \left(R_{n,z} - m_{i,z}\right)^2}. \tag{11}$$

Since the radar sensors in combination with the motion of the vehicle only span a synthetic aperture in the xy-plane as depicted in Fig. 2, the final SAR image is only processed in the xy-plane at the z-height of the radar sensors.

Consequently, according to equation (9), the assignment of the measured complex value to cell m_i is known. This complex pointer has to be rotated by the phase Φ according to the backprojection algorithm to achieve constructive or destructive overlapping.

$$\Phi = -\mathrm{j}2\pi \frac{f_\mathrm{start}}{c_0} \cdot 2\mathbf{r}\left(m_i|x_\mathrm{t}\right). \tag{12}$$

The backprojection algorithm according to (8) is applied not only for one measurement point and thus for one transmitted ramp but for all transmitted ramps of each frame. This creates a synthetic aperture, which allows highly accurate images of the environment.

For targets there is a constructive superposition of all pointers in the cell m_i and thus a high amplitude. For noise all pointers of the cell m_i point in different directions resulting in a destructive superposition which leads to a low amplitude in the cell m_i.

The approach leads to detectability problems of weak targets. Despite constructive superposition of the phasors the corresponding cell m_i represents low power and might be not identified as a target. Due to the approach of the BP algorithm as well as all SAR algorithms, the resulting image of the environment is always amplitude dependent. Therefore, sufficient dynamic range must be chosen to visualize the environment in order to detect both strong and weak targets. The problem of amplitude-based representations and calculation has been known for a long time and has already been investigated for target list-based grid maps. This problem can be avoided by probabilistic models resulting in an image of the environment which is almost amplitude independent and significantly more dependent on constructive and destructive superposition of the complex signals [8].

V. Probabilistic-Based SAR Processing

Probabilistic-based mappings of the environments provide significant advantages with respect to robustness and accuracy [6], [8], [7], [23]. In this case, each cell m_i does not represent the amplitude $\mathbf{G}(m_i)$ like in the amplitude-based SAR from Section IV, but a probability $\mathbf{p}(m_i)$. This probability ranges from 0 to 1. Free space is represented by the probability $p{=}0$, whereas targets are represented by the probability $p{=}1$. Areas where no information about the occupancy probability can be obtained are represented as $p{=}0.5$. This applies to cells outside the field of view (FoV) of the radar sensor as well as to cells that are not reliably detected in most frames.

In [24], [25] it was shown how basic probabilistic maps are generated. This general description is briefly shown below to introduce both the notation and the probabilistic representation. Since this description only includes the theory for real-valued grid maps, but not for complex-valued grid-maps like SAR imaging, the probabilities and models required for probabilistic SAR imaging must be redefined and derived.

Based on the range compressed fast time samples (5), probabilistic SAR processing is performed according to the green boxes in Fig. 3. Due to the complex-valued entries of the final SAR mappings, the probabilistic target modeling must be split into probabilistic amplitude modeling (Section A) and probabilistic phase modeling (Section B). This separate consideration is of great importance for the update step (Section C), since this update step is defined according to the descriptions of proabilistic

occupancy grid-maps only for real-valued data and thus has to be adapted [24], [25]. The free space model, which describes the probability of free space and thus creates a balance between occupied cells and free cells, is described in section E.

The probability that a cell m_i is occupied at time t based on all measurements z and all position data x up to time t is described by $\mathbf{p}\left(m_i|z_{1:t}, x_{1:t}\right)$. This probability can be described according to a binary Bayes filter with the assumption of a static environment with

$$\mathbf{p}\left(m_i|z_{1:\mathrm{t}}, x_{1:\mathrm{t}}\right) = \frac{\mathbf{p}\left(z_t|m_i, z_{1:\mathrm{t}-1}, x_{1:\mathrm{t}}\right)\mathbf{p}\left(m_i|z_{1:\mathrm{t}-1}, x_{1:\mathrm{t}}\right)}{\mathbf{p}\left(z_t|z_{1:\mathrm{t}-1}, x_{1:\mathrm{t}}\right)} \tag{13}$$

Using a Markov assumption, in the term $\mathbf{p}\left(z_t|m_i, z_{1:\mathrm{t}-1}, x_{1:\mathrm{t}}\right)$ previous observations can be neglected as soon as they are redundant. This redundancy is given by the knowledge of $\mathbf{p}(m_i)$. Thus all previous observations are already included and the equation simplifies to

$$\mathbf{p}\left(m_i|z_{1:\mathrm{t}}, x_{1:\mathrm{t}}\right) = \frac{\mathbf{p}\left(z_t|m_i, x_\mathrm{t}\right)\mathbf{p}\left(m_i|z_{1:\mathrm{t}-1}, x_{1:\mathrm{t}-1}\right)}{\mathbf{p}\left(z_t|z_{1:\mathrm{t}-1}, x_{1:\mathrm{t}}\right)} \tag{14}$$

Applying the Bayes and Markov rule multiple times yields the following term:

$$\begin{aligned}&\mathbf{p}\left(m_i|z_{1:\mathrm{t}}, x_{1:\mathrm{t}}\right)\\ &= \frac{\mathbf{p}\left(m_i|z_t, x_\mathrm{t}\right)\mathbf{p}\left(z_t|x_\mathrm{t}\right)\mathbf{p}\left(m_i|z_{1:\mathrm{t}-1}, x_{1:\mathrm{t}-1}\right)}{\mathbf{p}\left(m_i\right)\mathbf{p}\left(z_t|z_{1:\mathrm{t}-1}, x_{1:\mathrm{t}}\right)}.\end{aligned} \tag{15}$$

However, terms describing the probability $\mathbf{p}\left(z_t\right)$ cannot be determined directly, therefore they will be eliminated with the help of the counter event.

$$\mathbf{p}\left(\neg m_i|z_{1:\mathrm{t}}, x_{1:\mathrm{t}}\right) = 1 - \mathbf{p}\left(m_i|z_{1:\mathrm{t}}, x_{1:\mathrm{t}}\right) \tag{16}$$

$$= \frac{\mathbf{p}\left(\neg m_i|z_t, x_\mathrm{t}\right)\mathbf{p}\left(z_t|x_\mathrm{t}\right)\mathbf{p}\left(\neg m_i|z_{1:\mathrm{t}-1}, x_{1:\mathrm{t}-1}\right)}{\mathbf{p}\left(\neg m_i\right)\mathbf{p}\left(z_t|z_{1:\mathrm{t}-1}, x_{1:\mathrm{t}}\right)}. \tag{17}$$

The elimination of the non-determinable terms is performed by calculating the ratio of the occupancy probability (15) and the probability of the counter event (17). Based on this the occupancy probability of a cell is determined as follows:

$$\frac{\mathbf{p}\left(m_i|z_{1:\mathrm{t}}, x_{1:\mathrm{t}}\right)}{\mathbf{p}\left(\neg m_i|z_{1:\mathrm{t}}, x_{1:\mathrm{t}}\right)} = E_A \cdot E_B \cdot E_C \tag{18}$$

$$E_A = \frac{\mathbf{p}\left(m_i|z_t, x_\mathrm{t}\right)}{1 - \mathbf{p}\left(m_i|z_\mathrm{t}, x_\mathrm{t}\right)} \tag{19}$$

$$E_B = \frac{\mathbf{p}\left(m_i|z_{1:\mathrm{t}-1}, x_{1:\mathrm{t}-1}\right)}{1 - \mathbf{p}\left(m_i|z_{1:\mathrm{t}-1}, x_{1:\mathrm{t}-1}\right)} \tag{20}$$

$$E_C = \frac{1 - \mathbf{p}\left(m_i\right)}{\mathbf{p}\left(m_i\right)} \tag{21}$$

By rearranging, the probability of the cell m_i results in:

$$\mathbf{p}\left(m_i|z_{1:\mathrm{t}}, x_{1:\mathrm{t}}\right) = \frac{1}{\left(1 + E_A^{-1} \cdot E_B^{-1} \cdot E_C^{-1}\right)} \tag{22}$$

Using (22), the probability of cell m_i at time t can be determined based on the current measurement described by E_A and all previous measurements described by E_B. Since the map $\mathbf{m}$ is iteratively updated with the measured information of each ramp, E_B corresponds to the map at the previous time $t-1$. The variable E_C simply describes a priori information about the cell m_i.

Thus, to obtain a probabilistic representation of the environment, the probability $\mathbf{p}\left(m_i|z_\mathrm{t}, x_\mathrm{t}\right)$ must be modelled, which is derived in the following subsections. Once the cell probability for a cell m_i at each measurement time t is known the final probability of this cell based on all previous measurements $1{:}t-1$ can be determined.

Calculating a probabilistic map according to (22) for complex-valued SAR data is not possible without modifications, since the essential phase information of the SAR data cannot be included into the standard model. Consequently, in the following, complex probabilities p, with a magnitude and a phase are initially determined based on the measured raw radar data. This is done in two steps. First, the complex probability that the radar sensor detects a target is determined in Section A-D. However, since an environmental map is intended to represent the occupancy state of a cell rather than the detection probability, the complex probability that a cell represents a target is determined based on the detection probability in Section E.

A. Probabilistic Target Model

According to (9), due to the range assignment between frequency bins and grid-cells of the map $\mathbf{m}$, the corresponding complex range compressed data $\mathbf{A}$ is used for the backprojection in the case of the amplitude-based SAR algorithm at time t. This value can be split into a magnitude and a phase.

$$\mathbf{A}\left(m_i|z_\mathrm{t}, x_\mathrm{t}\right) = \left|\mathbf{A}\left(m_i|z_\mathrm{t}, x_\mathrm{t}\right)\right| \cdot \exp\left(\mathrm{j} \cdot \angle\mathbf{A}\left(m_i|z_\mathrm{t}, x_\mathrm{t}\right)\right) \tag{23}$$

In the first step, a probability is determined to replace the receive magnitude related radar cross section. The phase information is considered in more detail in Section B. The probability is determined based on the signal-to-noise ratio (SNR). The signal amplitude for a given cell m_i corresponds to $\left|\mathbf{A}\left(m_i|z_\mathrm{t}, x_\mathrm{t}\right)\right|$. The thermal noise for each range bin was estimated by measurements in free-space, allowing the calculation of the amplitude standard deviation σ_A for each intermediate frequency.

Moreover, if the components of a two-dimensional random vector are normally distributed and stochastically independent, the magnitude of the vector is Rayleigh-distributed [26], [27]. The probability density function $f(x|\sigma_A)$ of the Rayleigh distribution is given by

$$f\left(x|\sigma_A\right) = \begin{cases} \frac{x}{\sigma_A^2} e^{-\frac{x^2}{2\cdot\sigma_A^2}} & x \geq 0 \\ 0 & x < 0 \end{cases} \tag{24}$$

$f(x|\sigma_A)$ describes the probability density for received magnitudes x. For the radar sensors, whose σ_A is known, the probability is calculated that the measured amplitude $\left|\mathbf{A}\left(m_i|z_\mathrm{t}, x_\mathrm{t}\right)\right|$ for cell m_i at measurement time t is not caused by noise. This is the counter event of the

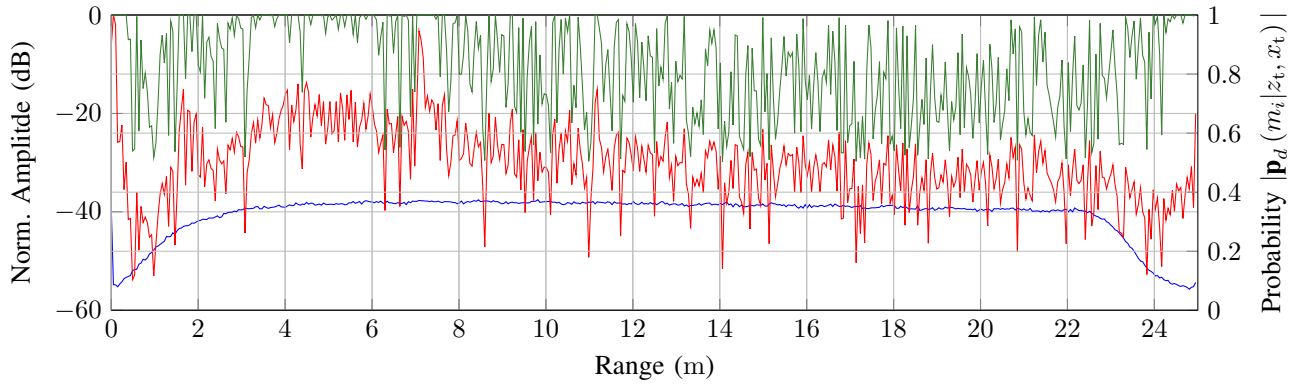

Fig. 4: Range spectrum by transforming the received fast time samples into the frequency domain (red) with corresponding target probability (green) and thermal noise of the sensor (blue) for each range bin.

probability that the magnitude of noise is greater than $|\mathbf{A}(m_i|z_t,x_t)|$ and can be determined by:

$$|\mathbf{p}_d(m_i|z_t,x_t)| = 1 - \int_{|\mathbf{A}(m_i|z_t,x_t)|}^{\infty} f(x|\sigma_A)\,\mathrm{d}x \quad (25)$$

$$= F(|\mathbf{A}(m_i|z_t,x_t)|) \quad (26)$$

For reasons of efficiency, the integral in (25) can be rewritten based on the cumulative distribution function $F(x)$ with

$$F(x) = \begin{cases} 1 - e^{-\frac{x^2}{2\sigma_A^2}} & x \geq 0 \\ 0 & x < 0 \end{cases} \quad (27)$$

$|\mathbf{p}_d(m_i|z_t,x_t)|$ describes the probability that a target located in the cell m_i at time t is detected by the radar sensor. For environmental mapping, however, the target probability and not the detection probability is of interest. Since $|\mathbf{p}(m_i|z_t,x_t)|$ describes the probability that a target exists in cell m_i and not the probability that the radar system detects a target, the detection probability $|\mathbf{p}_d(m_i|z_t,x_t)|$ has to be adjusted. This probability is approximated below based on two extreme cases.

First, the probability of a cell is p=0.5 if no information can be obtained about the cell. This is the case if the radar system cannot detect a target or the target is, for example weaker than the noise. This means if the detection probability p_d of the radar sensor for a target is 0 %, the existence probability p that there is a target is assumed to be p=0.5, since no information can be obtained. This assumption simplifies the following derivations but does not reflect the true relation between detection probability and occupancy probability. The calculation of the occupancy probability of a cell based on the detection probability is therefore adapted based on empirical measurements in Section E.

Second, the upper bound of the probability distribution is still at p=1. Based on these two assumptions, the target probability $|\mathbf{p}(m_i|z_t,x_t)|$ is approximated by the following equation based on the detection probability $|\mathbf{p}_d(m_i|z_t,x_t)|$:

$$|\mathbf{p}(m_i|z_t,x_t)| = \frac{|\mathbf{p}_d(m_i|z_t,x_t)|}{2} + 0.5 \quad (28)$$

In Fig. 4 the probability (green) for each distance is shown for the IF signal of a ramp in the frequency domain (red). The noise of the sensor, on the basis of which the probability per frequency bin is calculated, is shown in blue.

According to (23), the assigned measurement value for the cell m_i has both a magnitude and a phase, which is why the probability assigned to this cell must also contain phase information in order to perform SAR processing.

$$\mathbf{p}(m_i|z_t,x_t) = |\mathbf{p}(m_i|z_t,x_t)| \cdot \exp(j \cdot \angle\mathbf{p}(m_i|z_t,x_t))$$
$$= |\mathbf{p}(m_i|z_t,x_t)| \cdot \exp(j \cdot \angle\mathbf{A}(m_i|z_t,x_t)) \quad (29)$$

Thus, the probability corresponds to a complex probability, with a magnitude and a phase. While the magnitude is determined according to (28), the phase corresponds to the regular phase from (23), which is assigned to the frequency bin according to the FFT result $\mathbf{A}^t$.

B. Phase Model

According to (22), the occupancy probability for a specific cell based on the current measurement (t) is updated with the probability of the identical cell based on all previous measurements. However, this equation is only valid for real-valued probabilities. The calculated probability $\mathbf{p}(m_i|z_t,x_t)$ from (29) corresponds to a complex probability.

Since the radar measurements are affected by noise, and thus the received phase $\angle\mathbf{A}(m_i|z_t,x_t)$ is also noisy, this noise must be included in the target model. The radar sensors standard deviation of the phase is described in the following by σ_ϕ and is assumed to be Gaussian distributed. Therefore, each phase state represents a different probability, which at its maximum corresponds to the probability $|\mathbf{p}(m_i|z_t,x_t)|$ for the measured phase $\angle\mathbf{A}(m_i|z_t,x_t)$. The probability distribution for all phases before applying the BP algorithm is expressed as:

$$\mathbf{p}(m_i,\phi_{\text{in}}|z_t,x_t) = |\mathbf{p}(m_i,\phi_{\text{in}}|z_t,x_t)| \cdot \exp(j \cdot \phi_{\text{in}}) \quad (30)$$

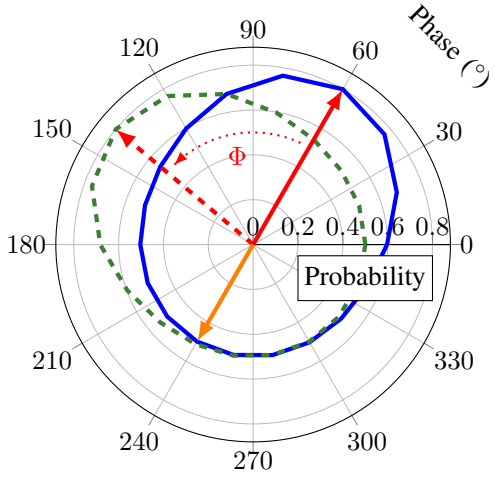

Fig. 5: Representation of the sampled complex probability $\mathbf{p}\left(m_i, \phi_{l,\text{in}} | z_\text{t}, x_\text{t}\right)$ in blue solid for L=18 states. Most probable phase represented as red arrow for 60°. Most implausible phase represented as orange arrow for 240°. Complex probability after applying the BP-algorithm $\mathbf{p}\left(m_i, \phi_{l,\text{out}} | z_\text{t}, x_\text{t}\right)$ represented in dashed green.

The magnitude of the probability for a given phase ϕ_in and a given cell m_i is modelled according to the Gaussian distribution by

$$\begin{aligned}\left|\mathbf{p}\left(m_i, \phi_\text{in} | z_\text{t}, x_\text{t}\right)\right| = &\frac{f\left(\phi_\text{in} | \mu_\phi, \sigma_\phi\right)}{\max\left(f\left(\phi_\text{in} | \mu_\phi, \sigma_\phi\right)\right)} \\ &\cdot \left(\left|\mathbf{p}\left(m_i | z_\text{t}, x_\text{t}\right)\right| - 0.5\right) + 0.5 \quad (31)\end{aligned}$$

In this case $f\left(\phi_\text{in} | \mu_\phi, \sigma_\phi\right)$ describes a wrapped Gaussian distribution which has an identical value at the phase values ϕ_in=0° and ϕ_in=360° due to the continuity condition. Thus $f\left(\phi_\text{in} | \mu_\phi, \sigma_\phi\right)$ is given by

$$f\left(\phi_\text{in} | \mu_\phi, \sigma_\phi\right) = \frac{1}{\sqrt{2\pi\sigma_\phi^2}} \sum_{c=-\infty}^{\infty} \exp\left(\frac{-\left(\phi_\text{in} - \mu_\phi - 2\pi c\right)^2}{2\sigma_\phi^2}\right) \quad (32)$$

The mean μ_ϕ corresponds to the measured phase for cell m_i and thus $\angle\mathbf{A}\left(m_i | z_\text{t}, x_\text{t}\right)$.

Since the probabilities corresponding to (22) can only be applied to real-valued and not to complex probabilities, the phase is sampled with L steps to have a real-valued probability $p\left(m_i, l_\text{in} | z_\text{t}, x_\text{t}\right)$ for each of the L phase states.

$$\begin{aligned}\mathbf{p}\left(m_i, l_\text{in} | z_\text{t}, x_\text{t}\right) &= \left|\mathbf{p}\left(m_i, l_\text{in} = \phi_\text{in} | z_\text{t}, x_\text{t}\right)\right| \quad (33)\\ l_\text{in} &= \left\{0, \frac{360°}{L}, 2 \cdot \frac{360°}{L}, \ldots, 360° - \frac{360°}{L}\right\}\end{aligned}$$

Thus for a certain cell m_i and a certain phase ϕ_in the probability has a real value. The cell m_i exists L times, each one representing one of the L possible phase states. The amplitude of each cell and each phase state can subsequently be used for the map update according to equation (22), since the cell itself represents the phase and the value of the cell the magnitude of the probability. This probability distribution for L possible phases of a cell m_i is shown in Fig. 5 in solid blue for L=18 steps, and thus a step size of 20°.

The figure illustrates the assignment of the highest probability for the measured phase $\angle\mathbf{A}\left(m_i | z_\text{t}, x_\text{t}\right)$, based on the FFT. This is illustrated by the red arrow, which indicates a probability of $\mathbf{p}\left(m_i, l_\text{in} | z_\text{t}, x_\text{t}\right)$ =0.8 for the phase state of l_in=$\angle\mathbf{A}\left(m_i | z_\text{t}, x_\text{t}\right)$ =60°. All other phase states, which are also possible due to measurement noise, have a lower probability. The lowest probability is the complementary phase to the measured phase, in this example 240°, which has only a probability of $\mathbf{p}\left(m_i, l_\text{in} | z_\text{t}, x_\text{t}\right)$ =0.5. This is represented by the orange pointer.

Thus, a real-valued probability is given for each possible phase state. The complex probability is therefore split into L real-valued probabilities for specific phases.

The selection of a suitable number of sampled phases is essential for the imaging quality and the computational efficiency, as will be shown in the measurement chapter VII. First, to achieve an ideal constructive update of all complex pointers of a target, a radar sensor with a phase standard deviation of σ_ϕ=0° and sampling with L=∞ steps would be required. However, since no component is noise-free, and thus σ_ϕ>0° holds, an ideal constructive update of all pointers of a target cannot occur due to the radar sensors noise. To avoid additional superposition errors due to phase sampling, the step size L should be chosen in a way that the discretization of the phase is in the same size as the phase noise. This is guaranteed if the maximum discretization error is as large as the maximum occurring phase error, which is assumed to be $\pm 3\sigma_\phi$ since this interval contains 99.73 % of all relevant target phases. Therefore, the following must hold:

$$\frac{360°}{L} \leq 2 \cdot 3\sigma_\phi \rightarrow L \geq \frac{360°}{6 \cdot \sigma_\phi} \quad (34)$$

C. Update Step

The update step, i.e. the step in which the current measurement $\mathbf{p}\left(m_i | z_\text{t}, x_\text{t}\right)$ taken at time t is combined with all previous measurements $\mathbf{p}\left(m_i | z_{1:\text{t}-1}, x_{1:\text{t}-1}\right)$, shows large differences between the amplitude-based SAR processing from Section IV and the probabilistic SAR processing from Section V. In contrast to conventional amplitude-based SAR processing according to (8), the complex pointers are not accumulated but probabilities are calculated for L different phase states, and updated at each time step t.

The update step always consists of two parts. The first part is the phase correction. This is performed by the backprojection algorithm and rotates the phase according to the distance between the radar sensor and the cell m_i according to (8). The second part is the map update, which combines the current probability of a cell with all previously gathered probabilities of this cell. In the ordinary amplitude-based SAR process, this map update is simply a summation, as described in (8).

The general steps are similar for probabilistic SAR. However, they have to be adapted. First, the complex

probabilities have to be phase-corrected accordingly. For this, the backprojection algorithm is used again. The difference to the conventional SAR processing is that not only the phase value of each cell m_i but also of each sampled phase l_{in} is rotated. Thus, the probability distribution from (30) changes after applying the BP algorithm to:

$$\begin{aligned}\mathbf{p}\left(m_i, \phi_{\text{out}}|z_{\text{t}}, x_{\text{t}}\right) =& |\mathbf{p}\left(m_i, \phi_{\text{in}}|z_{\text{t}}, x_{\text{t}}\right)| \\ & \cdot \exp\left(\mathrm{j}\cdot\left(\phi_{\text{in}} - \Phi\right)\right) \end{aligned} \tag{35}$$

The phase correction Φ is determined identically to (12) and is constant for each sampled phase ϕ_{in} of pixel m_i at time t and solely dependent in the distance between radar and cell m_i.

The general update formula from (22) must be extended such that identical cells m_i with identical output phases l_{out} are updated which expands it to the following equation.

$$\mathbf{p}\left(m_i, l_{\text{out}}|z_{1:\text{t}}, x_{1:\text{t}}\right) = \frac{1}{\left(1 + E_A^{-1}\cdot E_B^{-1}\cdot E_C^{-1}\right)} \tag{36}$$

$$E_A = \frac{\mathbf{p}\left(m_i, l_{\text{out}}|z_{\text{t}}, x_{\text{t}}\right)}{1 - \mathbf{p}\left(m_i, l_{\text{out}}|z_{\text{t}}, x_{\text{t}}\right)}$$

$$E_B = \frac{\mathbf{p}\left(m_i, l_{\text{out}}|z_{1:\text{t}-1}, x_{1:\text{t}-1}\right)}{1 - \mathbf{p}\left(m_i, l_{\text{out}}|z_{1:\text{t}-1}, x_{1:\text{t}-1}\right)}$$

$$E_C = \frac{1 - \mathbf{p}\left(m_i, l_{\text{out}}\right)}{\mathbf{p}\left(m_i, l_{\text{out}}\right)}$$

Since each cell represents only one real-valued scalar, i.e. only the magnitude of the probability $\mathbf{p}\left(m_i, \phi_{l,\text{out}}|z_{\text{t}}, x_{\text{t}}\right)$, and not the complex probability, the update step must take care of the correct assignment. Each cell update may only be performed for cells that have the same phase l_{out} after applying the BP algorithm according to (35).

For reasons of computational efficiency, it is useful to partially swap the order of the steps in this case. The phase correction Φ by the BP algorithm is identical for each of the L sampled phases at time t and doesn't depend on the initial phase. Therefore, it is reasonable to apply the BP algorithm to the complex probability from (29) and sample the phases from $0°$ to $360°$ afterwards.

In a matrix-based operation, this corresponds to having not only a 2D map with I cells, but a 3D map whose third dimension corresponds to the number of phase samples L. This means each 2D slice corresponds to a particular l_{out}. The first 2D slice corresponds to an output phase of l_{out}=0° whereas, the second 2D slice represents an output phase of l_{out}=20°. Thus, the assignment which is important for the other order (first sampling then applying the BP algorithm) can be neglected since it is inherently satisfied. The probability distribution $\mathbf{p}\left(m_i, l_{\text{out}}|z_{\text{t}}, x_{\text{t}}\right)$ is shown for an example phase rotation of Φ=80° as a dashed green line in Fig. 5.

An illustration of the whole principle is shown in Fig. 6 based on the example of Fig. 5. A map $\mathbf{m}$ with 16 cells is evaluated at cell m_i. This evaluated cell is shown in gray. After applying the BP algorithm, this cell contains a complex probability distribution $\mathbf{p}\left(m_i, l_{\text{out}}|z_{1:\text{t}}, x_{1:\text{t}}\right)$, which is shown in red. Since this cannot be used for the update step, the complex probability distribution is sampled with L values. The L=18 sampled probabilities are shown as arrows, color-coded according to phase. The amplitudes of each phase state are subsequently registered in the cell m_i in the respective SAR map representing the respective phase state l_{out}, which is exemplarily shown for three phase states. The L SAR maps can be represented as a 3D cube, where each cell of each slice represents the probability of a cell m_i for a certain phase state.

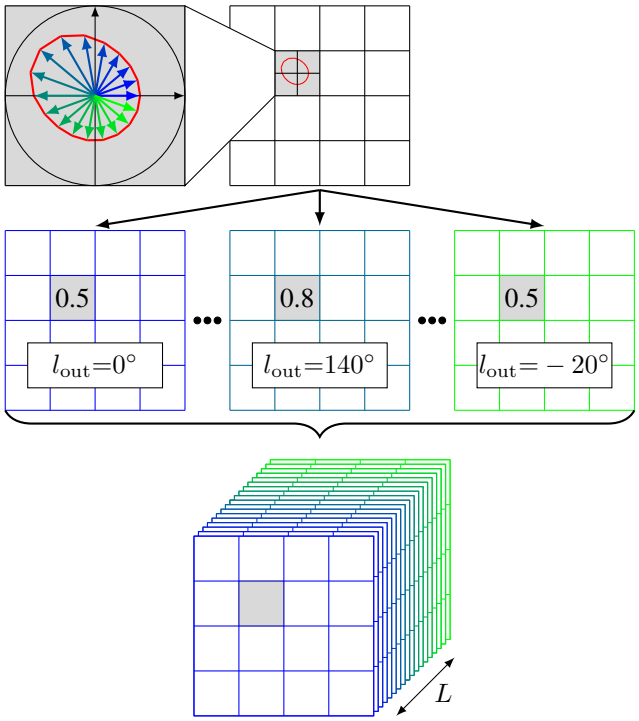

Fig. 6: Illustration of the update step based on a cell m_i shown in gray for a probability distribution $\mathbf{p}\left(m_i, l_{\text{out}}|z_{1:\text{t}}, x_{1:\text{t}}\right)$, shown in red and identical to the exemplary distribution from Fig. 5. L=18 samples of the probability distribution as color-coded pointers whose amplitudes are plotted in the phase-representing 2D SAR figures. Exemplary illustrated for three phase states l_{out}.

D. Numerical Error Prevention

With W frames and K ramps per frame, a total of $K{\cdot}W$ ramps are processed. Thus, in a typical application run, the probability of a cell m_i is updated several 100,000 times. This leads to numerical inaccuracies of the probabilities, which cause cells that have a probability $p{\approx}1$ to be rounded to p=1 and cells that have a probability $p{\approx}0$ to be rounded to p=0. Thus, these cells are set to wrong values. Furthermore, a cell which has a probability of exactly p=0 or p=1 will not change its probability value unless it is updated with a cell representing a probability of exactly p=1 or p=0.

To avoid these errors a log odd calculation must be used [28], which in the present case is applied as follows. Each

probability p is defined as a log odd ratio:

$$\Psi\left(m_i\right) = \log\left(\frac{p\left(m_i\right)}{1-p\left(m_i\right)}\right) \tag{37}$$

The update formula from (18) thus becomes a sum:

$$\begin{aligned}\boldsymbol{\Psi}\left(m_i, l_{\text{out}}|z_{1:\text{t}}, x_{1:\text{t}}\right) &= \Psi_A + \Psi_B + \Psi_C \\ \Psi_A &= \boldsymbol{\Psi}\left(m_i, l_{\text{out}}|z_{\text{t}}, x_{\text{t}}\right) \\ \Psi_B &= \boldsymbol{\Psi}\left(m_i, l_{\text{out}}|z_{1:\text{t}-1}, x_{1:\text{t}-1}\right) \\ \Psi_C &= \boldsymbol{\Psi}\left(m_i, l_{\text{out}}\right)\end{aligned} \tag{38}$$

This not only has numerical advantages, but also leads to more efficient calculations of the cell probabilities due to the addition in (38) instead of a multiplication. Due to the mandatory use of the log-odd method to calculate the probabilities for accurate computation, the following derivations are performed based on this probabilistic representation.

E. Balancing and Free-Space Model

The previous assumption according to chapter A is that a cell which is occupied has the probability p=1. In contrast, a cell should have the value p=0.5 if the radar sensor has not detected a target in this cell. As soon as the probability distribution $\mathbf{p}\left(m_i, \phi_{\text{out}}|z_{\text{t}}, x_{\text{t}}\right)$ represented in Fig. 5 for a cell m_i, it is noticeable that all probabilities are between p=0.5 and p=1. This results in updates with probabilities always larger than $p\geq$0.5. This leads to a total of $K{\cdot}W$ evaluated ramps which have probability $p\geq$0.5. However, the final map in this case consists only of cells which have probabilities of $p\geq$0.5. Because of the large number of ramps and frames per cell, it is very likely that all cells have a probability of $p\approx$1 in the end. Thus, every cell would be occupied and no realistic representation of the environment would be given. Therefore, two further normalization steps have to be performed to obtain a real image of the environment. First, a balance between integration and deintegration of the probabilities must be guaranteed. In order to ensure this balance, and thus the probability distribution between p=0.5 and p=1 not only for a measurement at time t, but also for all cells m_i and all steps 1:t, the probability distribution from (32) must be adjusted. The upper limit of p=1 is automatically reached over time as soon as probabilities p>0.5 are updated. The lower limit of p=0.5 after the evaluation of all 1:t measurements can only be reached if there is a balance between integration p>0.5 and deintegration p<0.5. This lower limit of p=0.5 is to be reached when the phases destructively overlap after azimuth compression and thus represent noise. Thus, only the lower limit of p=0.5 has to be taken into account.
The balance corresponds to a probability of p=0.5 which corresponds to a log-odd representation of Ψ=0. Since probabilistic processing is cell-independent using Markov assumptions [28], [29], this balance is computed separately for each cell.

$$\sum_{l=1}^{L}\left(\boldsymbol{\Psi}_{\boldsymbol{\zeta}}\left(m_i, \phi_{l,\text{out}}|z_{1:\text{t}}, x_{1:\text{t}}\right)\right) \overset{!}{=} 0 \tag{39}$$

The variable Ψ_ζ describes the log-odd probability of the probability p+ζ with

$$\Psi_\zeta\left(m_i\right) = \log\left(\frac{p\left(m_i\right)+\zeta}{1-\left(p\left(m_i\right)+\zeta\right)}\right), \tag{40}$$

where ζ corresponds only to a negative range shift in the polar coordinate system of the probability distribution from Fig. 5 over all L sampled phase states. The negative probability offset ζ must thus be added to each probability $\mathbf{p}\left(m_i, l_{\text{out}}|z_{\text{t}}, x_{\text{t}}\right)$ of the current measurement according to (41). The offset ζ cannot be determined by averaging Ψ, since these map a nonlinear function. Using an iterative procedure, the probability offset ζ is determined such that the sum over all L samples according to (39) equals zero. All derivations are based on assumptions for calculating the target probability based on the detection probability (28). If the radar sensor does not detect a target, the probability of the cell m_i must be p=0.5 since no information about the cell can be obtained based on the radar measurements. This assumption isn't valid and has to be corrected by means of empirical measurements to determine the target probability based on the detection probability. Expressed descriptively, ξ describes the probability that if the radar sensor does not detect a target, that no target exists. Thus, equation Ψ_A must be adapted from (38):

$$\boldsymbol{\Psi_A} = \boldsymbol{\Psi}_{\boldsymbol{\zeta},\boldsymbol{\xi}}\left(m_i, l_{\text{out}}|z_{\text{t}}, x_{\text{t}}\right). \tag{41}$$

The variable $\Psi_{\zeta,\xi}$ describes the log-odd probability of the probability p+ζ+ξ with

$$\Psi_{\zeta,\xi}\left(m_i\right) = \log\left(\frac{p\left(m_i\right)+\zeta+\xi}{1-\left(p\left(m_i\right)+\zeta+\xi\right)}\right). \tag{42}$$

This value was determined empirically for the selected radar sensors and is constant for all measurements as long as the sensor technology remains identical.

F. Final SAR-Image

According to Fig. 6, the SAR image of the environment does not consist of I pixels with the respective cells m_i like a conventional SAR image, but of L two-dimensional SAR images, each representing a different phase of the target in each cell. Thus, for each cell m_i and each sampled phase value l a real-valued probability p has been determined based on all measured values. However, since the ultimate concern is only whether a cell is occupied or not, and not the most probable phase, a simple maximum search in the third dimension reflecting the cell's occupancy probability Ψ_f is sufficient:

$$\boldsymbol{\Psi_f}\left(m_i, l_{\text{out}}|z_{1:\text{t}}, x_{1:\text{t}}\right) = \max_{l_{\text{out}}}\left(\boldsymbol{\Psi}\left(m_i, l_{\text{out}}|z_{1:\text{t}}, x_{1:\text{t}}\right)\right) \tag{43}$$



Fig. 7: Experimental system setup with two side-looking radar sensors on a car [6].



Fig. 8: Photograph of the measurement scene with several parked cars, hedges and trees, fences, roads, and gravel car parks. Approximated trajectory in red [6].

VI. Measurement Setup

The measurement setup to verify the theoretical considerations is shown in Fig. 7 and consists of $N{=}2$ laterally aligned incoherently connected chirp-sequence radar sensors [30].
Schematically, this measurement setup is shown in Fig. 2, where only the two turquoise sensors are used for the measurement evaluation. This indicates an orientation of $\phi_1{=}{-}90°$ and $\phi_2{=}90°$. High-precision ground-truth information in the half-wavelength range is required for SAR processing for both conventional SAR and probabilistic SAR.. In the automotive domain, this corresponds to approximately $2\,\mathrm{mm}$.
To ensure this position accuracy, a total station in combination with radar-based ego-motion estimation is used [31], [32]. A special prism is mounted on the vehicle roof in the middle of the rear axle. This prism can be tracked and localized in the 3D space via a laser with an accuracy of $2\,\mathrm{mm}$ using the total station. Radar-based ego-motion estimation additionally provides information about local x and y velocities as well as the yaw rate. The fusion of the global position data as well as the local velocity data determines the orientation of the vehicle in the global map. The measurements were performed on a parking lot displayed to Fig. 8.
For the time synchronization of the radar sensors an external trigger is used. This time synchronization is relevant to have accurate time stamps for the measurements, and to avoid interference between the radar sensors by using suitable frequency offsets [33]. The radar parameters are listed in table I.

TABLE I: Radar Parameters for Mapping

Parameter	**Value**	
	S_1	S_2
Start frequency f_0	77.6 GHz	77.63 GHz
Bandwidth f_B	3.07 GHz	
Ramp repetition time T_r	67 µs	
Sampling frequency f_s (IQ)	10 MHz	
Number of ramps	384	
Number of transmitters	1	
Number of receivers	4	
Measurement rate	37 Hz	

The high frame rate of $37\,\mathrm{Hz}$ allows to emit ramps almost without pause. The pause between the last ramp of the $(w{-}1)$-th frame and the first ramp of the w-th frame is only $1\,\mathrm{ms}$. To satisfy Nyquist's sampling theorem, the distances between two consecutive sensor positions must not exceed $\frac{\lambda}{2}$ [34]. Due to the four receive antennas, which have a distance of $\frac{\lambda}{2}$ to each other, this distance can be increased to $5 \cdot \frac{\lambda}{2}$, which corresponds to approximately $9.5\,\mathrm{mm}$ and thus a maximum vehicle speed of $v_\mathrm{max}{=}9.5\,\frac{\mathrm{m}}{\mathrm{s}}$ must not be exceeded.

VII. Measurement Results

In the following, Section A first presents the results of the probabilistic SAR algorithm for a parking lot drive. Three mapping types are compared to each other:

- Probabilistic SAR processing compared to (8)
- Ordinary amplitude-based SAR processing according to (38).
- Target list-based occupancy grid map corresponding to [8]

Then, in Section B, the phase progression over multiple evaluated ramps of three cells and thus three specific targets is examined. In particular, the comparison between probabilistic SAR update and conventional amplitude-based SAR update is addressed in this section. Finally, in C an analysis of the optimal phase sampling rate L is performed, since the computation time increases significantly with increasing number of phase states.

A. Multi Frame

The first comparison includes the evaluation of a total of $K{=}150$ frames with $W{=}384$ transmitted ramps and four receivers. Therefore, a total of approximately 230400 measurement ramps are processed. The result of probabilistic SAR processing is shown for $L{=}18$ phase samples in Fig. 9a.
Each cell directly illustrates the occupancy probability with probabilities between $p{=}0$ and $p{=}1$. A comparison with the photograph of the measurement environment from Fig. 8 illustrates that all relevant obstacles are clearly detectable on the probabilistic SAR image. Two vehicles

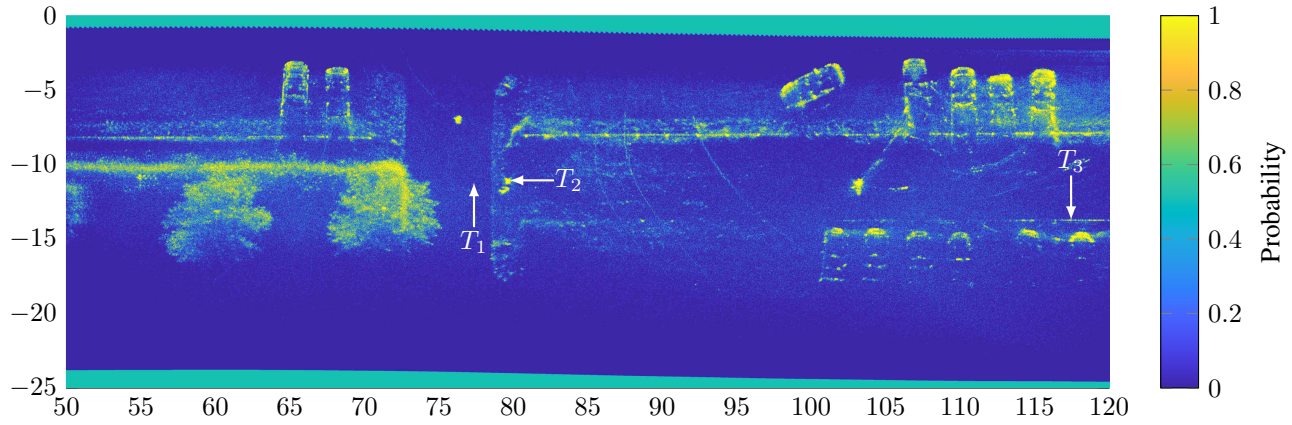

(a) Probabilistic SAR-Representation with L=18 phase states.

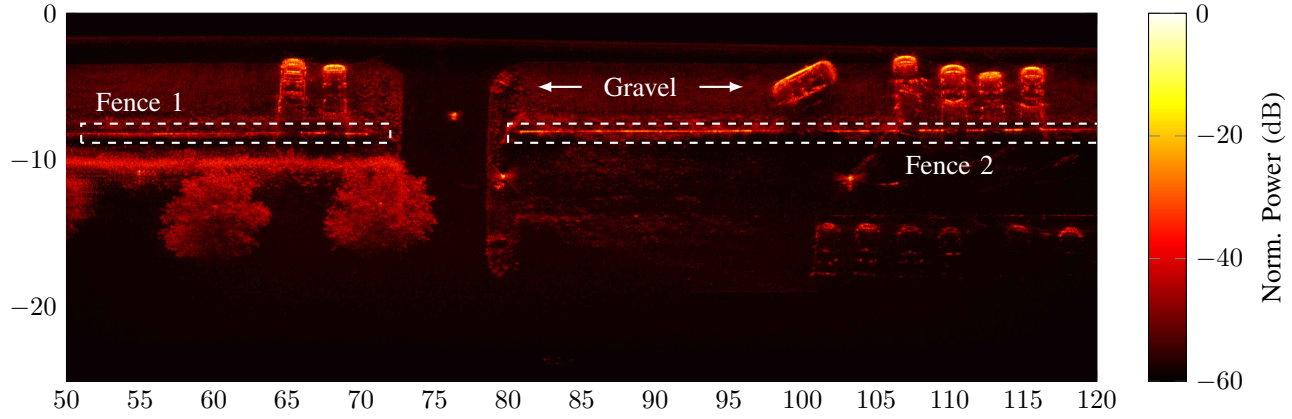

(b) Conventional amplitude-based SAR-Representation, [6].

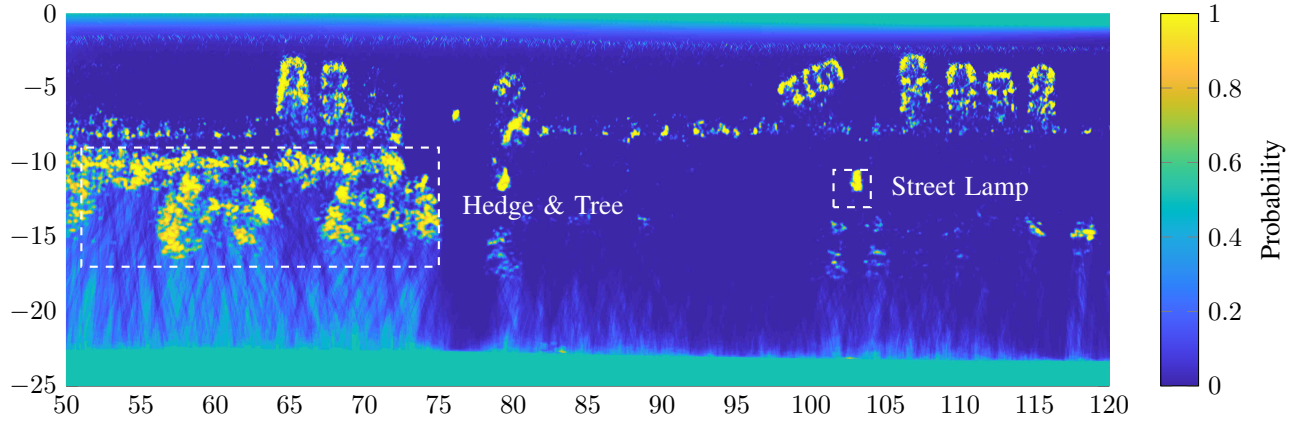

(c) Probabilistic occupancy grid map-based on target lists, [6].

Fig. 9: Comparison of three different mapping techniques. Top: probabilistic SAR processing yields a probability-based cell occupancy. Center: conventional and amplitude-based SAR-proecessing. Cell indicates the received power. Bottom: probability-based occupancy Grid-Map generated based on target lists. Cell represents the cell occupancy probability. x and y axis in m.

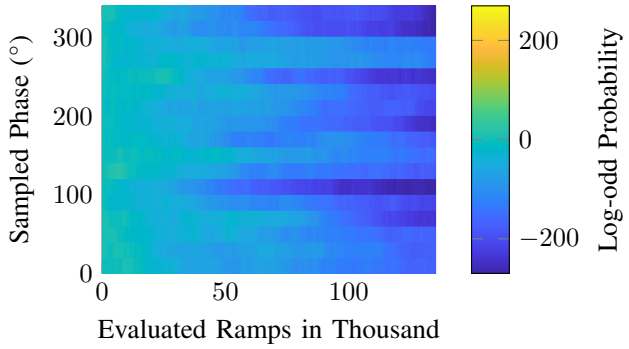

(a) Noise.

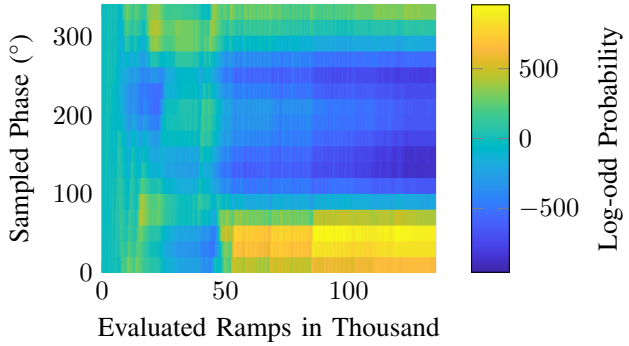

(b) Strongly reflective target.

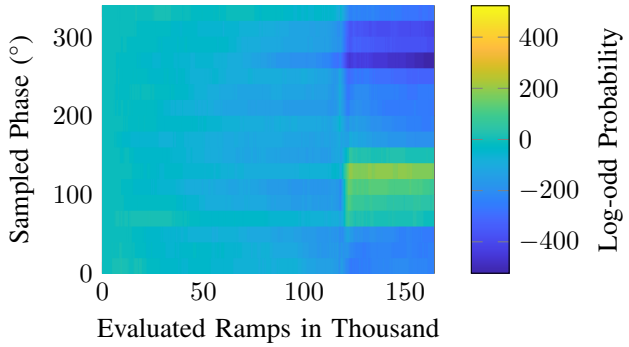

(c) Weakly reflective target.

Fig. 10: Probability distribution for multiple evaluated ramps and specific targets T_1, T_2, and T_3.

at $x{\approx}65\,\mathrm{m}$, as well as the five vehicles at $x{\approx}110\,\mathrm{m}$, one of them being rotated. Similarly, the two streetlights at $x{\approx}80\,\mathrm{m}$ and $x{\approx}103\,\mathrm{m}$ and the trees in the foreground can be clearly detected.

Based on the raw data used for probabilistic SAR processing, an amplitude-based SAR processing can also be performed. The amplitude-based SAR mapping based on these raw data is shown accordingly to [6] in Fig. 9b. In this case, the cells m_i do not indicate occupancy probabilities, but received logarithmic powers normalized to the maximum of the image. The above mentioned obstacles, vehicles, fences, trees etc., can be detected as well. However, the detection is only possible with correctly chosen dynamics of the z-axis, which is limited to $60\,\mathrm{dB}$ for this purpose. The dynamic of $60\,\mathrm{dB}$ is no longer sufficient to identify also weak targets if a strongly reflecting target, for example a large corner reflector exist. This problem can already be seen with the dynamic range of $60\,\mathrm{dB}$. The parked cars in the second row at $y{\approx}-15\,\mathrm{m}$ are already $50\,\mathrm{dB}$ weaker and almost not identifiable anymore.

In addition, it is important for autonomous systems whether the areas are passable or not. Thus, a threshold search would still have to be performed on the amplitude-based SAR mapping to estimate the occupancy state of the cell. In the probabilistic SAR processing from Fig. 9a, this subsequent step is unnecessary, since the occupancy probability P is determined directly. The occupancy is almost independent of the detected received power due to the applied algorithm. This can be shown particularly well at two selected cells T_2 and T_3. While T_2 represents a scattering point of the lamppost, T_3 reflects the wooden bar of a fence. From Fig. 9b, it can be seen that the targets have a power difference of more than $50\,\mathrm{dB}$. If this is compared with the probability of the two cells an identical probability of $p_{T_2}{\approx}p_{T_3}{\approx}1$ is determined. Thus, due to the probability-based calculation, an almost amplitude independent and robust occupancy representation is given without loosing the integration gain of SAR processing.

An additional important advantage of the probabilistic representation is the certainty that a target or the free space is detected. In the ordinary SAR processing from Fig. 9b no distinction can be made between unoccupied cells and cells outside the FoV of the radar sensor. Both cells are black and thus do not represent back-reflected energy. In both the probabilistic OGM of Fig. 9c and the probabilistic OSAR in Fig. 9a, this is directly indicated by the two turquoise regions $y{\geq}{-}1\,\mathrm{m}$ and $y{\leq}{-}23\,\mathrm{m}$. These areas represent the occupancy probability $p{=}0.5$ whereby no information can be obtained about these cells and no free area is wrongly assumed.

A brief comparison to another probabilistic mapping method, state of the art occupancy grid maps (T-OGMs), also illustrates the advantages of this probabilistic mapping method. T-OGMs are target list-based mapping methods, which, unlike SAR processing, are not based on raw data. Fig. 9c shows such an T-OGM based on target lists extracted from raw data. The T-OGM was performed according to [8]. A comparison between probabilistic raw data processing (SAR) from Fig. 9a and probabilistic processing of target lists (OGM) from Fig. 9c shows clear differences. While free parking spaces can also be determined in OGM by directly estimating the state of each cell, weakly reflective targets can only be identified to a limited extent. Since only the integration gain of all $K{=}384$ emitted ramps can be used in target list generation and not frame spanning integration gain as in SAR processing, targets like the fence slats are not detected at all, but only the fence posts. In addition, the angle estimation accuracy is limited by the limited aperture size and SNR. With only four receive antennas this leads to the fact that a separation of the targets, for

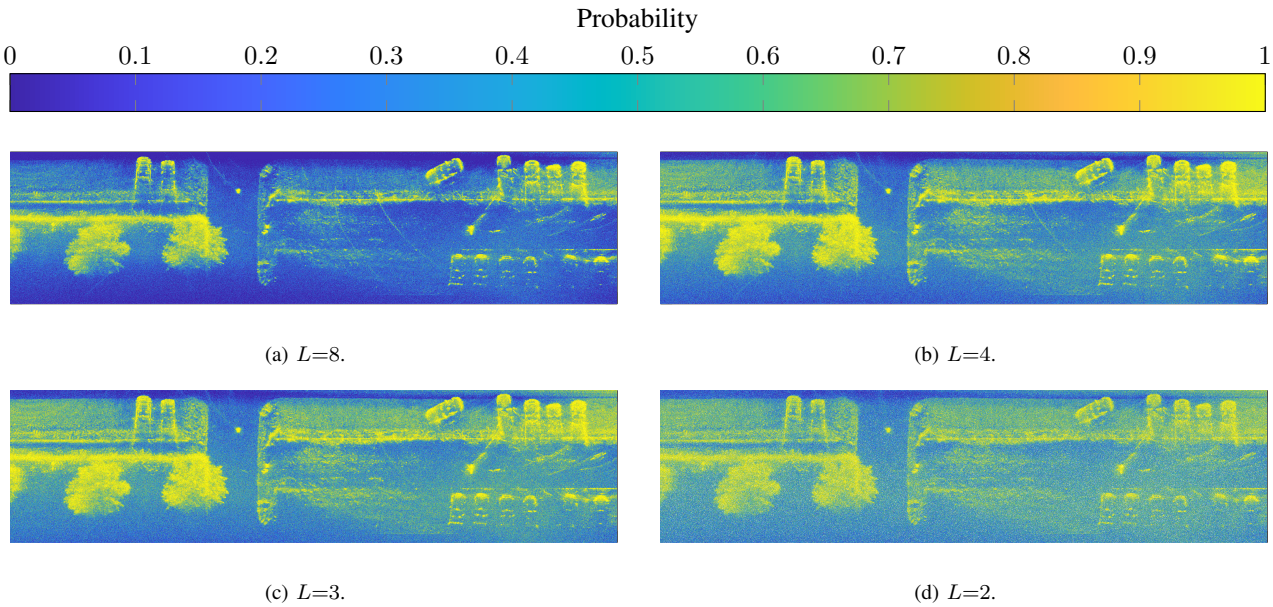

(a) L=8.

(b) L=4.

(c) L=3.

(d) L=2.

Fig. 11: Resulting probabilistic SAR representation for different number of phase states of the sampled complex probability. Equivalent coordinate system to Fig. 9.

example the lantern at $(80\,\mathrm{m}|-12\,\mathrm{m})$ and the stone at $(80\,\mathrm{m}|-12.5\,\mathrm{m})$ is not possible. In probabilistic SAR processing just as in amplitude-based SAR processing, the large synthetic aperture allows for significantly higher separability in the azimuth direction on the imaging strip of

$$\delta_{\mathrm{SAR}} = \frac{\Lambda}{2}, \tag{44}$$

where Λ is the length of the physical antenna aperture, not the synthetic one. Although the gap is very small, it can be clearly identified as a free space in the probabilistic SAR mapping.

The significantly increased accuracy of SAR processing makes it possible to distinguish the surface roughness of pavements, which makes it possible to clearly distinguish the asphalted road from the gravelled parking area [6]. For the probabilistic SAR processing, this high accuracy is also maintained, which means different roughnesses can be clearly recognized with this probabilistic calculation as well Fig. 9a. The gravel areas representing the parking bays are clearly distinguishable from the paved road due to the different probabilities despite the probabilistic representation.

To determine the imaging accuracy, the total station was utilized to determine the position with mm-accuracy of the lanterns at approximately x=80 m, y=−12 m and x=103 m, y=−12 m. For both the probabilistic SAR mapping from Fig. 9a and the conventional SAR mapping from Fig. 9b, the root mean square error (RMSE) is 1.2 cm. The target-list-based OGM cannot guarantee this accuracy of target localization due to the much smaller aperture and thus smaller angle estimate, increasing the RMSE by the factor of 5 to 5.4 cm.

B. Comparison of Phase Progressions

At each time step t the probabilities are calculated for L different phase states. This differs from conventional amplitude-based SAR processing using (8) where the complex pointers are just accumulated. The probabilistic update step for different times t is illustrated with the help of the three marked targets T_1, T_2, and T_3 from Fig. 9a in Fig. 10.

The three investigated targets differ in the back-reflected power. While T_1 represents the asphalt and thus no target, the targets T_2 represent a strongly reflecting metallic lantern and T_3 a weakly reflecting wooden fence at larger distance. The probability profile for all L phase states of the containing cell m_i is plotted over all measurement points. Only those measurement points are shown for which the respective target is within the field of view (FoV and $r_{\max}$) of the radar sensor.

First, the target T_1 is considered, whose phase response over the evaluated ramps is visualized in Fig. 10a. This target only represents noise, since there is no obstacle at this position. As soon as the target is in the radar sensor's field of view, i.e. at the time of the first transmitted ramp, the probabilities, for each phase state are set to p=0.5 or in log-odd notation Ψ=0.

With more evaluated ramps, the probability for all L phase states is increasingly reduced, because the measured phase $\angle\mathbf{p}\left(m_i, l_{\mathrm{out}}|z_{\mathrm{t}}, x_{\mathrm{t}}\right)$ is too diffuse after applying the BP algorithm. Thus, after about 150,000 evaluated ramps, there is a negative log-odd probability for each phase state. According to (43), the cell probability of cell m_i corresponds to the maximum of all L=18 phase states at the last measurement time, which corresponds to a log-

odd value of -127 for the phase value $280°$ and thus to a probability of $p{\approx}0$.
For the target T_2, shown in Fig. 10b, which represents a real target, the metallic lamppost, a different probability profile is recognizable. For the first transmitted ramps, initialization is also visible with a probability of $p{=}0.5$. With more evaluated ramps it becomes clearer that containing cell has a phase state of $60°$, since the log-odd probability is highest here and corresponds to a probability of $p{\approx}1$. The probabilities accumulate to the final phase state not before the 50000 evaluated ramp. This is because the lamppost is obscured by the two parked cars at $(68\,\mathrm{m}|{-}6\,\mathrm{m})$.
The robustness advantages of weakly reflective targets in probabilistic SAR processing could be clearly demonstrated. The influence on the map update and the occupancy probability is shown in Fig. 10c for the target T_3. This is not a point target like T_2 is, but merely a spot on the wooden fence, which is also more distant and therefore reflects less power overall. Analogous to the target T_2, the occlusion by the parked cars in the foreground is again noticeable. Here, the fence is occluded for almost $60\,\%$ of the synthetic aperture. In combination with the generally worse reflecting target and the larger distance this leads to a clearly lower maximum log-odd probability of only 160, compared to a log-odd probability of the target T_2 of almost 1000. If these two log-odd ratios are converted into a probability according to (37), a value of $p{\approx}1$ results for both.

C. Ideal Sampling of the Phase

SAR processing is generally more time-consuming than other mapping options, but in exchange offers significantly higher mapping accuracies as discussed in Section A. Regardless of the probabilistic update steps in probabilistic SAR compared to amplitude-based SAR, probabilistic SAR has an L times higher computational complexity since an entire SAR image must be computed for each of the L phase states. The probabilistic SAR processing yields different results for different number of phase states. This is shown in Fig. 11 for four different phase symmetries $L{=}\{2,3,4,8\}$.
All four figures are based on the same raw data as Fig. 9a, which however was calculated using $L{=}18$ phase states and thus based on $20°$ steps. Fig. 11a has been processed based on $L{=}8$ phase states and thus based on $45°$ steps. Compared to Fig. 9a, an increased noise is noticeable, which, does not have too much impact on the resulting map. As soon as only $L{=}\{2,3,4\}$ phase states are processed according to Fig. 11b, Fig. 11c and Fig. 11d, the noise increases significantly. Some cells show a probability of $p{=}1$ although there is no target at this position. This is due to the insufficiently sampled phase. With only $L{=}2$ phase states and thus a sampling in $180°$ steps, measured complex pointers, which for example have a phase difference of $179°$, and thus theoretically lead to a destructive overlay, are updated in the same cell, with their full probability according to (38). Thus, in the case of insufficient phase states, the phases of the targets constructively overlap, although they should actually destructively overlap in the worst-case scenario. As a result, many cells are wrongly assigned the probability $p{=}1$.

VIII. CONCLUSION

A fundamentally new method for probabilistic processing radars raw data for generating high-resolution SAR images of the environment has been presented in this paper. The presented probabilistic SAR processing combines the advantages of ordinary amplitude-based SAR processing, based on raw data, and conventional probability-based occupancy grid maps, based on target lists. The accuracy, resolution, and integration gain of SAR, can be combined with the robustness, direct state estimation of each cell, and amplitude-independent detection of probabilistic representations and calculations. A measurement comparison based on identical raw data between the probabilistic SAR processing, ordinary amplitude-based SAR processing and a state of the art target list-based occupancy grid map illustrated this. Targets are represented with a probability of $p{=}1$ regardless of their RCS, without compromising resolution or finest details. The independence of the presented algorithm of the used radar system architectures allows this probabilistic SAR processing for all radar sensors and application contributions.

REFERENCES

[1] I. Bilik, "Comparative Analysis of Radar and Lidar Technologies for Automotive Applications," *IEEE Intell. Transp. Syst. Mag.*, Jan. 2022.

[2] F. Roos, J. Bechter, C. Knill, B. Schweizer, and C. Waldschmidt, "Radar Sensors for Autonomous Driving: Modulation Schemes and Interference Mitigation," *IEEE Microw. Mag.*, vol. 20, pp. 58–72, 2019.

[3] M. Gottinger, M. Hoffmann, M. Christmann, M. Schütz, F. Kirsch, P. Gulden, and M. Vossiek, "Coherent Automotive Radar Networks: The Next Generation of Radar-Based Imaging and Mapping," *IEEE J. Microw.*, vol. 1, no. 1, pp. 149–163, 2021.

[4] C. Waldschmidt, J. Hasch, and W. Menzel, "Automotive Radar — From First Efforts to Future Systems," *IEEE J. Microw.*, vol. 1, pp. 135–148, 2021.

[5] S. Kong, F. Shi, C. Wang, and C. Xu, "Point Cloud Generation From Multiple Angles of Voxel Grids," *IEEE Access*, vol. 7, pp. 160 436–160 448, 2019.

[6] T. Grebner, P. Schoeder, V. Janoudi, and C. Waldschmidt, "Radar-Based Mapping of the Environment: Occupancy Grid-Map Versus SAR," *IEEE Microwave and Wireless Components Letters*, vol. 32, no. 3, pp. 253–256, 2022.

[7] K. Werber, M. Rapp, J. Klappstein, M. Hahn, J. Dickmann, K. Dietmayer, and C. Waldschmidt, "Automotive Radar Gridmap Representations," in *IEEE MTT-S Int. Conf. Microw. Intell. Mobil. (ICMIM)*, 2015, pp. 1–4.

[8] P. Hügler, T. Grebner, C. Knill, and C. Waldschmidt, "UAV-Borne 2-D and 3-D Radar-Based Grid Mapping," *IEEE Geosci. Remote Sens. Lett.*, pp. 1–5, 2020.

[9] M. Steiner, T. Grebner, and C. Waldschmidt, "Millimeter-Wave SAR-Imaging With Radar Networks Based on Radar Self-Localization," *IEEE Trans. Microw. Theory Techn.*, vol. 68, no. 11, pp. 4652–4661, 2020.

[10] V. T. Vu, T. K. Sjogren, and M. I. Pettersson, "A Comparison between Fast Factorized Backprojection and Frequency-Domain Algorithms in UWB Lowfrequency SAR," in *Int. Geosci. Remote Sens. Symp. (IGARSS)*, vol. 4, 2008, pp. IV – 1284–IV – 1287.

[11] G. Wang, F. Qi, Z. Liu, C. Liu, C. Xing, and W. Ning, "Comparison Between Back Projection Algorithm and Range Migration Algorithm in Terahertz Imaging," *IEEE Access*, vol. 8, pp. 18 772–18 777, 2020.

[12] G.-C. Sun, Y. Liu, J. Xiang, W. Liu, M. Xing, and J. Chen, "Spaceborne Synthetic Aperture Radar Imaging Algorithms: An overview," *IEEE Geosci. Remote Sens. Mag.*, vol. 10, no. 1, pp. 161–184, 2022.

[13] A. G. Stove, "Linear FMCW Radar Techniques," *IEE Proc. F Radar Signal Process.*, vol. 139, no. 5, pp. 343–350, 1992.

[14] H. Rohling and M.-M. Meinecke, "Waveform Design Principles for Automotive Radar Systems," in *CIE Int. Conf. on Radar Proc. (Cat No.01TH8559)*. IEEE, 2001, pp. 1–4.

[15] A. Meta, P. Hoogeboom, and L. Ligthart, "Signal Processing for FMCW SAR," *IEEE Trans. Geosci. Remote Sens.*, vol. 45, pp. 3519 – 3532, 12 2007.

[16] ——, "Correction of the effects induced by the continuous motion in airborne FMCW SAR," in *IEEE Conference on Radar*, 2006, pp. 8 pp.–.

[17] X. V. Yang, V. M. Patel, and A. P. Petropulu, "Spaceborne SAR Antenna Size Reduction Enabled by Compressive Sampling," in *IEEE Global Conference on Signal and Information Processing (GlobalSIP)*, 2016, pp. 297–301.

[18] S. Tebaldini, M. Manzoni, D. Tagliaferri, M. Rizzi, A. V. Monti-Guarnieri, C. M. Prati, U. Spagnolini, M. Nicoli, I. Russo, and C. Mazzucco, "Sensing the Urban Environment by Automotive SAR Imaging: Potentials and Challenges," *Remote Sensing*, vol. 14, no. 15, 2022.

[19] S. Wang, V. Nolden, G. Briese, S. A. Lang, and N. Pohl, "Effects of Radar Position Errors on Near Range Ultrawideband 3D-SAR Imaging," in *Proceedings of EUSAR: 11th European Conference on Synthetic Aperture Radar*, Jun. 2016, pp. 1–4.

[20] J. C. Curlander and R. N. Mcdonough, "Synthetic Aperture Radar: Systems and Signal Processing," 1991.

[21] O. Frey, C. Magnard, M. Ruegg, and E. Meier, "Focusing of Airborne Synthetic Aperture Radar Data From Highly Nonlinear Flight Tracks," *IEEE Trans. Geosci. Remote Sens.*, vol. 47, no. 6, pp. 1844–1858, 2009.

[22] L. Ulander, H. Hellsten, and G. Stenstrom, "Synthetic-Aperture Radar Processing Using Fast Factorized Back-Projection," *IEEE Trans. Aerosp. Electron. Syst.*, vol. 39, no. 3, pp. 760–776, 2003.

[23] R. Prophet, H. Stark, M. Hoffmann, C. Sturm, and M. Vossiek, "Adaptions for Automotive Radar Based Occupancy Gridmaps," *IEEE MTT-S International Conference on Microwaves for Intelligent Mobility (ICMIM)*, pp. 1–4, 2018.

[24] S. Thrun, "Learning Occupancy Grids with Forward Models," in *IEEE Int. Conf. Intell. Robots Syst.*, vol. 3, 2001, pp. 1676–1681 vol.3.

[25] ——, "Learning Metric-Topological Maps for Indoor Mobile Robot Navigation," *Artif. Intell.*, vol. 99, no. 1, pp. 21–71, 1998.

[26] W. Stone, R. Brock, and K. Hammerle, "On the First Probability of Detection by a Radar Receiver System," *IEEE Trans. Inf. Theory*, vol. 5, no. 1, pp. 9–11, 1959.

[27] M. Shor and N. Levanon, "Performances of Order Statistics CFAR," *IEEE Trans. Aerosp. Electron. Syst.*, vol. 27, no. 2, pp. 214–224, 1991.

[28] S. Thrun, W. Burgard, and D. Fox, *Probabilistic robotics*. Cambridge, Mass.: MIT Press, 2005.

[29] L. E. Baum and T. Petrie, "Statistical Inference for Probabilistic Functions of Finite State Markov Chains," *The annals of mathematical statistics*, vol. 37, no. 6, pp. 1554–1563, 1966.

[30] V. Winkler, "Range Doppler Detection for Automotive FMCW Radars," in *Eur. Microw. Conf. (EuMC)*, Oct. 2007, pp. 1445–1448.

[31] *Trimble Universale Total Station SPS930*, 2018.

[32] T. Grebner, P. Schoeder, F. Konrad, and C. Waldschmidt, "Instantaneous Ego-Motion Estimation based on Ambiguous Velocity Information within a Network of Radar Sensors," in *14th German Microwave Conference (GeMiC)*, 2022, pp. 140–143.

[33] M. Steiner, M. Keller, J. Geiß, M. Vossiek, and C. Waldschmidt, "Synchronization of Radar Sensors in a Network Based on Inter-Sensor Interference," in *16th European Radar Conference (EuRAD)*, 2019, pp. 229–232.

[34] C. Shannon, "Communication in the Presence of Noise," *Proceedings of the IRE*, vol. 37, no. 1, pp. 10–21, jan 1949.



Timo Grebner (Graduate Student Member, IEEE) received the master's degree in electrical engineering from Ulm University, Ulm, Germany, in 2019, where he is currently pursuing the Ph.D. degree in electrical engineering at the Institute of Microwave Engineering. In 2018, he was an Intern with Sony, Japan.

His current research interest includes the creation of high-resolution occupancy gridmaps by highaccuracy ego-motion estimations in a distributed and collaborative radar sensor topology.

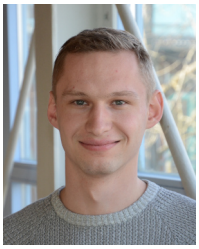

Alexander Grathwohl (Graduate Student Member, IEEE) received the master's degree in electrical engineering from Ulm University, Ulm, Germany, in 2019, where he is currently pursuing the Ph.D. degree in electrical engineering at the Institute of Microwave Engineering with a focus on airborne GPSAR systems and their application for humanitarian demining. From 2017 to 2018, he was an Intern with EAA, Bosch Sensortec, Sunnyvale, CA, USA.



Pirmin Schoeder (Graduate Student Member, IEEE) received the B.Sc. and M.Sc. degrees in 2017 and 2019, respectively, in electrical engineering from the University of Ulm, Ulm, Germany, where he is currently working toward the Ph.D. degree with the Institute of Microwave Engineering. In 2019, he was an Intern with Rohde & Schwarz, Singapore.

His current research interests include system concepts and signal processing for radar target simulators.



Vinzenz Janoudi received the M.Sc. degree in electrical engineering from the University of Applied Sciences of Karlsruhe, Karlsruhe, Germany, and the M.Eng degree from Toronto Metropolitan University, Toronto, ON, Canada, in 2018 and 2019, respectively. He is currently working toward the Ph.D. degree in electrical engineering with the Institute of Microwave Engineering, University Ulm, Ulm, Germany.

In 2015 and 2016, he was with Rohde & Schwarz, Munich, as a Bachelor Thesis Student and Development Engineer for software defined radio waveforms. In 2018, he was with Bosch Corporate Research as a Master thesis Student in the field of distributed source coding. From 2019 to 2020, he was with PLATH Group as a Development Engineer for signal intelligence receivers and direction finders. Since 2020, he has been a Research Assistant with the University Ulm. His research interests include communication systems, stochastic signal processing, system concepts for radar networks in the automotive sector, and the accompanying signal processing.



Christian Waldschmidt (Fellow, IEEE) received the Dipl.-Ing. (M.S.E.E.) and the Dr.-Ing. (Ph.D.E.E.) degrees from the University Karlsruhe, Karlsruhe, Germany, in 2001 and 2004, respectively.

From 2001 to 2004, he was a Research Assistant with the Institut für Höchstfrequenztechnik and Elektronik, Universität Karlsruhe. Since 2004, he has been with Robert Bosch GmbH, in the business units Corporate Research and Chassis Systems. He was heading different research and development teams in microwave engineering, rf-sensing, and automotive radar. In 2013, he returned to academia. He was appointed as the Director of the Institute of Microwave Engineering, University Ulm, Ulm, Germany, as Full Professor. He has authored or coauthored more than 200 scientific publications and more than 20 patents. His research topics include on radar and rf-sensing, mm-wave and submillimeterwave engineering, antennas and antenna arrays, and rf and array signal processing. He is a Member of the Executive Committee Board of the German MTT/AP joint chapter, and Member of the German Information Technology Society. He is Chair of the IEEE MTT-29 Technical Committee on Microwave Aerospace Systems and was the Chair of MTT-27 Technical Committee on Wireless Enabled Automotive and Vehicular Applications. He was a two-time TPC Chair and General Chair of the IEEE MTT International Conference on Microwaves for Intelligent Mobility. Since 2018, he has been an Associate Editor for IEEE MTT MICROWAVE WIRELESS COMPONENTS LETTERS. He is a reviewer for multiple IEEE transactions and many IEEE conferences in the field of microwaves. He was co-recipient of 13 best paper awards since 2014.